Assessment of the 3D Localization of Metallic Nanoparticles in Pd/SiO_2 Cogelled Catalysts by Electron Tomography

Cédric J. Gommes,*,† Krijn de Jong,‡ Jean-Paul Pirard,† and Silvia Blacher†

Department of Chemical Engineering, Université de Liège, B6a, Allée du 6 août, 3, 4000 Liège, Belgium, and Department of Inorganic Chemistry and Catalysis, Utrecht University, Sorbonnelaan 16, 3584 CA Utrecht, The Netherlands

Received June 22, 2005. In Final Form: September 29, 2005

The purpose of this study is to analyze the localization of palladium nanoparticles within their silica support, in two heterogeneous catalysts synthesized by the sol−gel process, with different metal loadings. Electron tomography demonstrates that the palladium particles are localized deep inside the silica skeleton. The use of digital image analysis further shows that the dispersion of palladium is optimal in the sample with the lowest loading. The particles are regularly spaced in the middle of the silica skeleton, with a distance between them comparable to the diameter of the struts of silica.

1. Introduction

A central problem in the characterization of heterogeneous catalysts is the analysis of the dispersion of active sites within the passive support. As a rule of thumb, the better the dispersion, the more active is the catalyst. In the case of metallic catalysts, the dispersion of the active metal nanoparticles is usually estimated through the chemisorption of an appropriate molecule or through their mean size obtained, e.g., by analyzing the width of X-ray crystallographic peaks. These physicochemical data can generally be validated by electron microscopy and in particular transmission electron microscopy (TEM). The analysis of these characterization data is however not devoid of ambiguity. For instance, chemisorption and X-ray analysis only conveys some partial information on the size of the metallic particles but not on their spatial distribution within the support. Some insight into the spatial arrangement of the active sites can be gained through TEM observation, but the interpretation of the micrographs is generally not unique because only projections of the objects are analyzed.

The present study deals with a metallic catalyst supported on silica, synthesized by a sol−gel method, according to a method developed by Heinrichs et al.[1−4] and initially explored by the group of Schubert to disperse a metal in a silica matrix.[5,6] According to this technique, an organically substituted alkoxide of the type $(RO)_3Si-X-A$, in which a functional organic group A, able to form a chelate with a cation of a metal such as palladium, silver, copper, etc., is linked to the hydrolyzable silyl group $(RO)_3Si$ via an inert and hydrolytically stable spacer X. The co-condensation of such a molecule with a network-forming reagent such as TEOS, $Si(OC_2H_5)_4$, results in materials in which the metal is anchored to the SiO_2 matrix. The method was used to synthesize Pd/SiO_2, Ag/SiO_2, and Cu/SiO_2 monometallic catalysts[1,7−10] and $Pd-Ag/SiO_2$ and $Pd-Cu/SiO_2$ bimetallic catalysts.[2,11] The Pd catalysts were found to be active for the hydrodechlorination of 1,2-dichloroethane mainly into ethane,[7] and the addition of Ag and Cu in the bimetallic catalysts was shown to increase the selectivity toward ethylene.[11] The monometallic Ag or Cu catalysts are active and highly selective for the benzene oxidation into H_2O and CO_2 only.[7]

For low metal loadings, about 1 wt % metal, the overall structure of these materials, after calcination and reduction, is that of metallic crystallites finely dispersed inside a macroporous aerogel-like structure. As assessed by CO or O_2 chemisorption measurements, the typical size of the metallic particles is 3 nm, which compares also well with the width of X-ray diffraction peaks and with direct microscopic observation.[7] Interestingly, it seems from TEM that the metallic crystallites in these materials are buried inside the silica skeleton,[1,2,7−11] which seems also to be compatible with some preliminary XPS analysis.[12] Notwithstanding their localization, the crystallites are accessible, as demonstrated by the chemisorption measurements and by the high catalytic activity. For higher metal loadings, a significant amount of metal is also present outside of the silica skeleton, under the form of a large crystallite with a width of a few tens of nanometers (e.g., ref 7).

The present study focuses on two Pd/SiO_2 samples synthesized as described previously[7] and representative of xerogel catalysts with well-dispersed and badly dis-

* To whom correspondence should be addressed. Telephone: +32-(0)4-366-2951. Fax: +32-(0)4-366-3545. E-mail: cedric.gommes@ulg.ac.be.

† Université de Liège.

‡ Utrecht University.

(1) Heinrichs, B.; Noville, F.; Pirard, J.-P. *J. Catal*. **1997**, *170*, 366.
(2) Heinrichs, B.; Delhez, P.; Schoebrechts, J.-P.; Pirard, J.-P. *J. Catal.* **1997**, *172*, 322.
(3) Heinrichs, B.; Pirard, J.-P.; Pirard, R. U.S. Patent 5,538,931, 1996.
(4) Delhez, P.; Heinrichs, B.; Pirard, J.-P.; Schoebrechts, J.-P. U.S. Patent, 6,072,096, 2000.
(5) Breitscheidel, B.; Zieder, J.; Schubert, U. *Chem. Mater*. **1991**, *3*, 559.
(6) Mörke, W.; Lamber, R.; Schubert, U.; Breitscheidel, B. *Chem. Mater*. **1994**, *6*, 1659.
(7) Lambert, S.; Cellier, C.; Grange, P.; Pirard, J.-P.; Heinrichs, B. *J. Catal*. **2004**, *221*, 335.
(8) Lambert, S.; Sacco, L.; Heinrichs, B.; Noels, A.; Pirard, J.-P. *J. Non-Cryst. Solids* **2004**, *343*, 109.
(9) Sacco, L.; Lambert, S.; Pirard, J.-P.; Noels, A. F. *J. Catal*. **2005**, *232*, 51.
(10) Lambert, S.; Polard, J.-F.; Pirard, J.-P.; Heinrichs, B. *Appl. Catal., B* **2004**, *50*, 127.
(11) Lambert, S.; Ferauche, F.; Brasseur, A.; Pirard, J.-P.; Heinrichs, B. *Catal. Today* **2005**, *100*, 283.
(12) Heinrichs, B.; Lambert, S.; Alié, C.; Pirard, J.-P.; Beketov, G.; Nehasil, V.; Kruse, N. *Stud. Surf. Sci. Catal*. **2002**, *143*, 25.

10.1021/la051682c CCC: $30.25 © 2005 American Chemical Society
Published on Web 11/15/2005

Table 1. Synthesis of the Pd/SiO_2 Xerogel Catalysts

	$Pd(acac)_2$ (g)	EDAS (mL)	TEOS (mL)	0.18 M NH_3 (mL)	C_2H_5OH (mL)
Pd1.1	0.097	0.14	12.3	5.0	32.6
Pd3.1	0.206	0.30	12.1	5.0	32.6

persed metal, respectively. In the present paper, the dispersion of the metallic particles within the silica support is analyzed by using electron tomography (3DTEM), which enables 3D images of microstructures to be obtained at the nanometer scale, and is receiving a growing interest in both materials science[13−16] and biology.[17] In the present work, to fully exploit the unique structural information obtained through 3DTEM, the images are analyzed using digital image analysis techniques with methods derived from spatial statistics. In particular, the issue of the localization of the particles with respect to the silica skeleton is addressed. The morphological data extracted from the 3D images are analyzed in the light of previously published textural information obtained on these catalysts.

2. Experimental Procedures

2.1. Preparation of the Xerogel Catalysts. The general method for preparing the Pd/SiO_2 xerogel catalysts analyzed in this paper has been described elsewhere.[7] Palladium acetylacetonate powder [$Pd(acac)_2$] and 3-(2 aminoethyl)aminopropyltrimethoxysilane (EDAS) are mixed together in ethanol. The slurry is then stirred at room temperature for about a half an hour, until a clear yellow solution is obtained, which is characteristic of a palladium complex. After the addition of tetraethoxysilane (TEOS), a solution of aqueous 0.18 M NH_3 in ethanol is added to the mixture. The vessel is then closed, and the solution is left aging for 7 days at 60 °C.

Afterward, the samples are dried in an oven where, over a period of a week, the temperature is raised from 60 to 150 °C and the pressure is lowered to 1200 Pa. The dry samples were calcined under an air flow, with a progressive increase of temperature from room temperature to 400 °C with a heating rate of 120 °C/h, and maintained at this temperature for 12 h. Reduction of the samples was performed under a H_2 flow; the samples were heated to 350 °C at a rate of 350 °C/h and maintained for 3 h at that temperature.

Two samples are analyzed in the present study, whose synthesis conditions are reported in Table 1. The same hydrolysis ratio, $H_2O/(TEOS + {}^3/_4\,EDAS) = 5$, dilution ratio, ethanol/(TEOS + EDAS) = 10, and complexation ratio, $EDAS/Pd(acac)_2 = 2$, were used for the two samples, and only the amount of Pd salt was modified. To make the comparison with previous work conducted on these samples easier,[7] they are called Pd1.1 and Pd3.1, in which the names are derived from their actual metal loading (1.1 and 3.1 wt %). These values are slightly higher than the theoretical loading that could be estimated from Table 1, owing probably to a loss of unpolymerized TEOS or EDAS during the drying.[7]

2.2. Electron Microscopy. For preparing the microscopy grids, the samples were first crushed in a mortar into very fine powder. A small amount of powder was then dispersed in ethanol for a few minutes in a sonication bath. The dispersion was finally let rest for another few minutes; a drop of the supernatant was put on the microscopy grid; and the solvent was evaporated.

The TEM observation was performed on a Tenai20FEG microscope (FEI Co.) operating at 200 kV. Projection images under sample rotation angles from −70° to +70° (at 1° increments) were automatically acquired with Inspect3D (FEI) on a slow scan CCD camera (Gatan). At a magnification of 25000×, the nominal pixel size in the CCD images was 0.7 nm.

Figure 1 represents three TEM micrographs of a fragment of Pd1.1 catalyst viewed under three different angles corresponding to ca. −20°, 0°, and +20°. On these images, the translucent gray object is the silica skeleton and the black dots are the palladium nanoparticles, which are mostly visible in the insets. From a single of these micrographs, the exact positioning of the Pd particles would be impossible to assess, because only a projection of the structure is accessible. However, when these three micrographs are compared, corresponding to projections along three different directions, it can be inferred that the visible Pd particles are located inside the silica and not on its surface.

Actually, the information contained in the 2D projections of a given object along an infinity of different directions is equivalent to that contained in the original 3D object. In this study, the 3D structure was gained by weighted backprojection, after alignment of the projections with respect to a common origin by fiducial markers by the IMOD software.[18] The observed low contrast between silica and carbon foil can possibly be addressed to sample contamination (carbon buildup) during acquisition. Because of the limited angular range in the projections (missing wedge of information in Fourier space), image features (e.g., the metal particles) appear elongated in the z direction of the reconstructions. Moreover, certain particles also appeared bent because of imperfect alignment of the projection images.

The main purpose of the present study is not the characterization the Pd particles themselves, which problem has been satisfactorily addressed by chemisorption and X-ray diffraction[7,10], but their localization with respect to the silica skeleton, for which problem 3DTEM is the ideal experimental technique. On the low-resolution tomograms used in the present study, the localization of the Pd particles is unambiguous. Because the size of the Pd nanoparticles is only slightly larger than a few voxels, their shape is poorly represented. The advantage of using low-resolution images is the large number of metal particles that can be analyzed at once. Typically, a single analyzed 3D image contains about 1000 particles, which can easily be handled with digital image analysis, and it enables statistically significant conclusions to be drawn.

2.3. Image Segmentation. The structure of the palladium catalysts is triphasic because it contains (i) the silica skeleton, (ii) the pore space, and (iii) the palladium nanoparticles. However, the raw data obtained from electron tomography only provides us with gray level images corresponding to the electron optical density of the various points of the structure. It is the purpose of the segmentation step to take advantage of the different gray levels associated with these phases to discriminate to which phase each voxel of the 3D image belongs. The segmentation is a necessary preliminary step to extract quantitative morphological information out of the 3D tomograms. The image analysis presented in this paper was performed using the Matlab software together with its Image Processing toolbox and the SDC morphology toolbox.

Although the images of the samples obtained by electron tomography are 3D by nature, processing them using general 3D tools would present some difficulties. Typically, the analyzed 3D images are a piling up of ca. 400 images of 400 × 400 pixels, and when treated in double precision, such a structure requires approximately 512 MB. Processing such an image as a single object would be very time-consuming. Moreover, this would also make it difficult to assess the accuracy the image analysis, because it is hard to visualize 3D triphasic systems at each step of the processing. Therefore, the segmentation of the images was performed sequentially on groups of neighboring slices, as described hereafter.

The first step of the segmentation is the discrimination between the silica skeleton and pore space, which is illustrated in Figure 2. Figure 2a is a typical 2D image of the interior of a fragment of the Pd/SiO_2 xerogel catalyst, corresponding to a slice taken out of the 3D image. Before the image processing is described, it is useful to recall that the visual appearance of an image is not

(13) Koster, A. J.; Ziese, U.; Verkleij, A. J.; Janssen, A. H.; de Jong, K. P. *J. Phys. Chem. B* **2000**, *104*, 9368.
(14) Janssen, A. H.; Yang, C.-M.; Wang, Y.; Schuth, F.; Koster, A. J.; de Jong, K. P. *J. Phys. Chem. B* **2003**, *107*, 10552.
(15) Ziese, U.; de Jong, K. P.; Koster, A. J. *Appl. Catal., A* **2004**, *260*, 71.
(16) Weyland, M.; Midgley, P. A. *Materials Today* **2004**, *7*, 32.
(17) Frank, J., Ed.; *Electron Tomography: Three-Dimensional Imaging with Transmission Electron Microscope*; Kluwer Academic: Norwell, MA, 1992.
(18) Mastronarde, D. N. *J. Struct. Biol.* **1997**, *120*, 343.

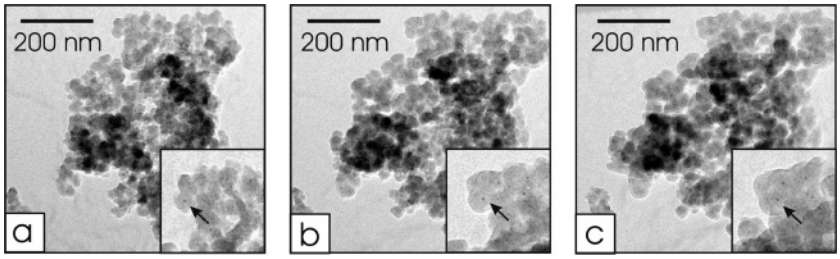

Figure 1. Examples of projections of a fragment of sample Pd1.1 along three different angles corresponding to ca. −20° (a), 0° (b), and +20° (c). The insets are magnified views in which it appears that the particles are located inside the silica.

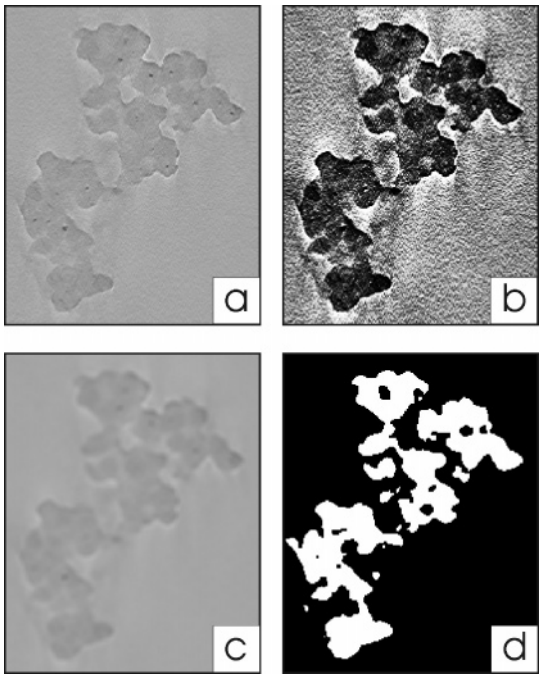

Figure 2. Segmentation of the silica skeleton: (a) original 2D slice taken out of the 3D image; (b) same image after histogram equalization, showing the connectivity of the silica; (c) low-pass filtered image; and (d) final binary image after thresholding and closing.

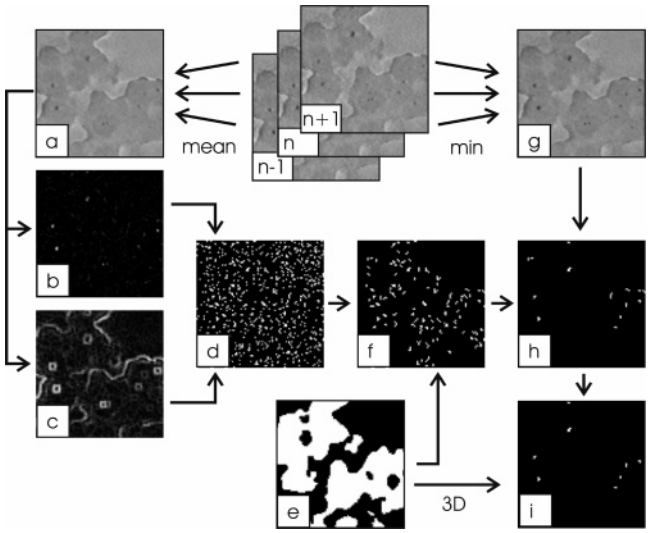

Figure 3. Segmentation of the palladium particles within the nth slice. The image (a) is denoised by averaging three consecutive slices $n - 1$ to $n + 1$. A top-hat filter (b) and an erosion gradient (c) are applied to the image to highlight its local minima. A binary image of the minima (d) is obtained by assigning the value 1 to all pixels where the top hat is larger than the erosion gradient. This image is then intersected with the silica skeleton (e), and all objects smaller than 1 pixel and larger than 25 pixels are removed (f). The contrast of the particles in the gray level image is increased by considering the minimum value of slices $n - 1$ to $n + 1$ (g). Only the objects of image f whose intensity in image g is lower than a given threshold are retained (h). Finally, all 3D objects touching the surface of the silica skeleton are removed (i).

necessarily representative of its actual content, especially for poorly contrasted images such as in Figure 2a. The reason for this is that the eye does not perceive with an equal acuity all gray levels. A so-called histogram equalization[19] was therefore applied to the original image to enhance the contrast and to help the reader judge the value of the image processing (Figure 2b). The processing is as follows. (i) A low pass filter is first applied to the original slice (Figure 2a) to denoise it and to smooth the palladium particles out. To that purpose, the four adjacent slices surrounding that of Figure 2a are averaged pixel by pixel. The resulting image is then passed through a 5×5 pixel-averaging filter (Figure 2c). (ii) The filtered image is afterward binarized by assigning the value 1 to all pixels whose intensity is below a given threshold and 0 to the others. Practically, the optimum threshold is calculated from the histogram of gray levels of the image, using the method of Ostu.[20] A single threshold is calculated from a representative 2D slice taken in the middle of the 3D image, and the same value is used for all of the other slices. (iii) After this thresholding step, some small black holes are still present in the image and they are removed by applying a closing filter.[19,21] The final binary image of the silica skeleton is that of Figure 2d. The shape of the binary object is globally accurate, as can be seen by comparing parts b and d of Figure 2. It should also be stressed that the binary 2D image in Figure 2d should not be considered individually, because it belongs to a 3D structure obtained by piling up similar images. For instance, the parts of Figure 2d that first seem to be disconnected from one another actually belong to a single connected 3D binary object.

The segmentation of the palladium particles requires a more convoluted processing because of the low resolution of the images. The particles are only a few pixels wide, and elaborate methods are needed to discriminate them from the noise. The used method is presented in Figure 3. It takes advantage of both nonlocal properties of the images based on the comparison of each pixel with its neighborhood, and local properties based on the intensity of any given pixel. These two complementary approaches correspond to the left and right branches of Figure 3, respectively. As a very first step, the images are denoised by averaging three adjacent slices (Figure 3a). To highlight the local minima (nonlocal property) of the resulting image, a so-called top-hat filter is applied (Figure 3b).[21] The top-hat image, I_{th}, contains bright spots that are generally not isolated, and when a threshold is applied to it, it would generally not result in isolated compact objects. Therefore, the erosion gradient, I_{eg}, of the original image is also computed (Figure 3c).[21] From this operation, a bright boundary is created around each local minimum of the original image. Creating a new image whose pixels have the value 1 wherever I_{th} is larger than I_{eg} results in a binary image in which all of the local minima are clearly disconnected (Figure 3d). Obviously, only a small fraction of the minima visible in Figure 3d

(19) Russ, J. C. *The Image Processing Handbook*, 4th ed.; CRC Press: Boca Raton, FL, 2002.
(20) Otsu, N. *IEEE Trans. Syst. Man. Cybernet* **1979**, *9*, 62.
(21) Soille, P. *Morphological Image Analysis, Principles, and Application*; Springer: Berlin, Germany, 1999.

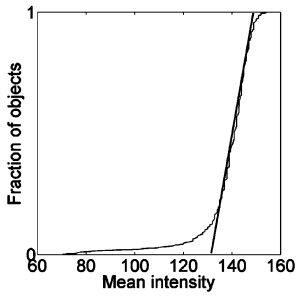

Figure 4. Example of cumulative distribution of the objects in Figure 3f as a function of their intensity in Figure 3g. The intersection of the line with the horizontal axis is the threshold used to discriminate between palladium particles and spurious local minima.

corresponds to Pd particles. To eliminate the minima located in the pore space, the minima image is intersected with the binary image of the silica skeleton previously computed as described in Figure 2 (Figure 3e). Furthermore, the disconnected objects containing only 1 pixel or more than 25 pixels are also removed. The use of these two size criteria is motivated by the observation that the largest visible palladium particles seldom exceed 5 pixels in size and that 1 pixel is the resolution limit of the image. The resulting image is in Figure 3f. The selection of the palladium particles among all of the objects of Figure 3f is based on the local intensity of the original image, which has not been exploited yet at this stage. Because the palladium particles are the darkest objects in the images, their contrast can be enhanced by considering the minimal value of the intensity over the same initial three slices (Figure 3g). For each object present in image 3f, the intensity of the corresponding pixels in image g of Figure 3 is averaged. Figure 4 plots a typical example of cumulative distribution of the number of objects in image f of Figure 3 as a function of their mean intensity in image g of Figure 3. This distribution clearly provides evidence of two kinds of objects. The most numerous are the bright objects, characterized by a mean intensity of about 140, coexisting with a smaller population of darker objects. The intensity threshold that enables the discrimination between these two populations is obtained by performing a linear regression on the high intensity part of the distribution and by intersecting the line with the intensity axis. In the particular case of Figure 4, the obtained threshold is close to 130. When only the objects of Figure 3f whose mean intensity is lower than this threshold are retained, one obtains Figure 3h. In this image, there are still some spurious objects that correspond to the border of the silica skeleton. Because it is difficult to discriminate between these shadow-like objects (Figure 3a) and actual particles, all of the objects touching the border were removed. This latter step is actually performed in 3D: all of the rough images of the palladium particles (similar to Figure 3h) were piled up, and the 3D objects touching the border of the 3D silica skeleton were removed. Figure 3i is a slice out of the final 3D binary image of the palladium nanoparticles.

To better visualize the characteristics of the obtained binary image of the palladium particles, three consecutive slices are displayed in Figure 5. The distance between these slices is two pixels; i.e., only one slice of two was represented. The central image (Figure 5b) is the same detail of Figure 2a as in Figure 3. Most of the Pd particles were correctly segmented. Two very small particles however, circled in Figure 5b, were lost during the segmentation procedure. This loss results from the elimination of all objects with a size of 1 pixel (parts d−f of Figure 3). It cannot be avoided without introducing a large number of spurious objects in the images. A given object in Figure 5e (indicated by an arrow) seems to be absent in the corresponding gray level image. It is however present in a neighboring slice (Figure 5c). It is obvious that the detection of the Pd particles by the proposed methodology is not as accurate as it could have been using high-resolution 3DTEM (e.g., ref 16). It must however be stressed that, in this latter case, at most a few tens of Pd particles could have been considered, while in the present study, about 1000 particles are detected per 3D image and several such images are used to characterize a single sample. It is merely a matter of strategy to choose either to describe precisely the particles out of a poor sampling or to coarsely describe the particles out of a sampling that could be statistically representative. The second option was chosen in the present study.

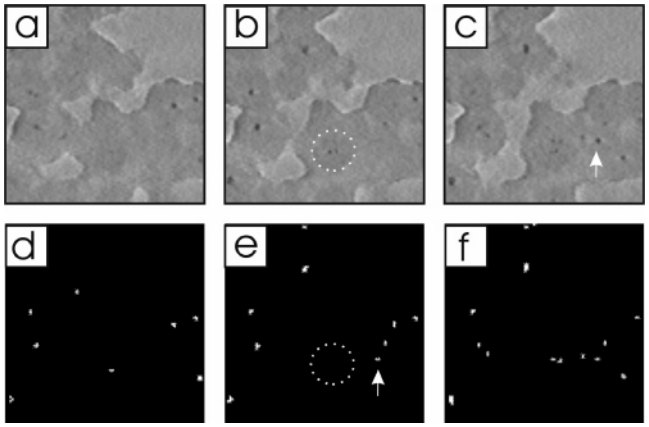

Figure 5. Detail of three slices: $n - 2$ (a), n (b), and $n + 2$ (c) and of their segmented versions (d−f). The two particles circled in b are smaller than 1 pixel and were lost during the segmentation. Some particles appear in the binary image, but they are visible mostly in neighboring slices (arrows in e and c).

3. Results

3.1. Qualitative Results. Binary images of the silica skeleton and of the palladium particles, obtained by the method described previously, are represented in Figure 6. In this representation, the complex structure of the silica skeleton can be visualized as well as the distribution of palladium particles inside the silica. Owing to the morphological complexity of the amorphous silica support, a reliable description of the structure cannot be obtained through a simple visual inspection, and a statistical approach is required. It is the purpose of this section to describe how quantitative morphological characteristics were extracted from these images, to better compare the structure of the two analyzed catalysts. For each sample, the analysis was conducted on 5 tomograms similar to those of Figure 6, which accounts for approximately 3000 Pd nanoparticles for each sample.

In sample Pd3.1, the large Pd particles that were previously observed by 2D TEM[7] are also detected by 3DTEM. Figure 7 displays such a large particle, whose size is larger than about 10 nm. From the few similar large particles observed in the tomograms, it seems that, contrary to the small particles, they are mainly located at the surface of the silica. It should be stressed that the binary image of Figure 7 was segmented by manually selecting the appropriate thresholds. Indeed, the large particles are not detected by the automatic segmentation procedure described in section 2.3, because they are not revealed by the top-hat or gradient filter, which only highlights the small features of the images. For these reasons, the large particles are not taken into account for the statistical analysis.

Because the actual macroscopic metal loading of the samples is known,[7] it is useful to compare it with the local metal content of the tomograms. An order of magnitude of the palladium content of the catalysts can be obtained as the ratio of the number of voxels in the Pd image over the number of voxels in the silica image and correcting this ratio by an estimation of the densities of these two phases. Taking 12 g/cm^3 as the density of palladium and 2 g/cm^3 as the density of silica leads to a metallic loading of ca. 3 wt % for both Pd1.1 and Pd3.1. Although the order

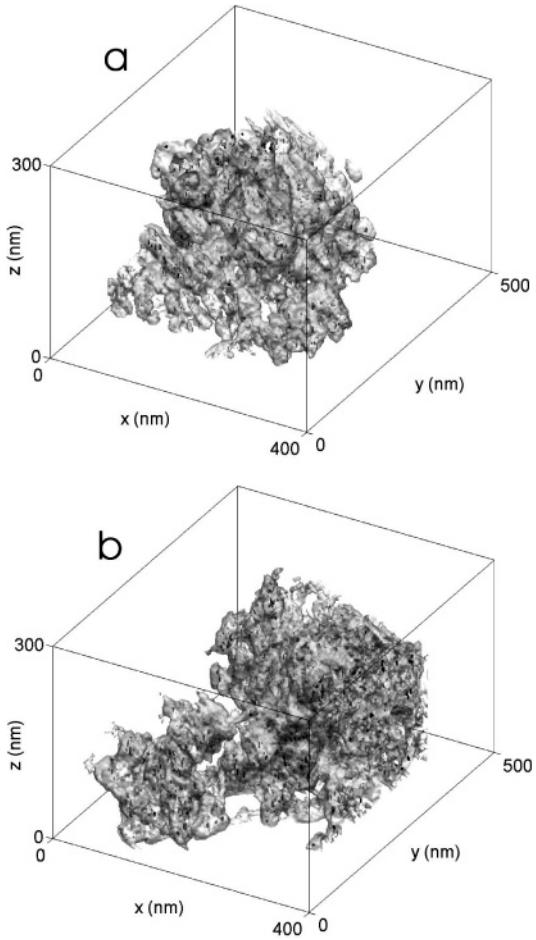

Figure 6. Examples of 3D views of the binary images of Pd particles and of silica, for samples Pd1.1 (a) and Pd3.1 (b). The semitransparent bright gray sheet is the surface of the silica skeleton, and the black dots are the palladium particles. Note that the samples were cut so that part of the interior of the silica is visible.

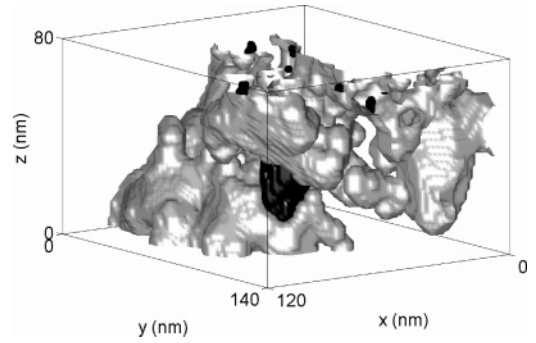

Figure 7. Example of a large Pd particle in sample Pd3.1. Contrary to the small particles, these large particles are outside of the silica skeleton.

of magnitude is correct, this value overestimates the loading of Pd1.1 that should be closer to 1 wt %. It is likely that this error results from an overestimation of the size of the particles. As can be seen in Figure 6, most of the particles have a shape that is elongated in the *z* direction, which is an artifact due to the missing wedge (in Fourier space, caused by the limited angular range) of single axis tomography. Although the same effect is visible for the images of Pd3.1, it seems that the overestimation of the metal loading is not so large for this sample. This issue is related in the presence of undetected very large Pd particles, and it is further addressed in the Discussion.

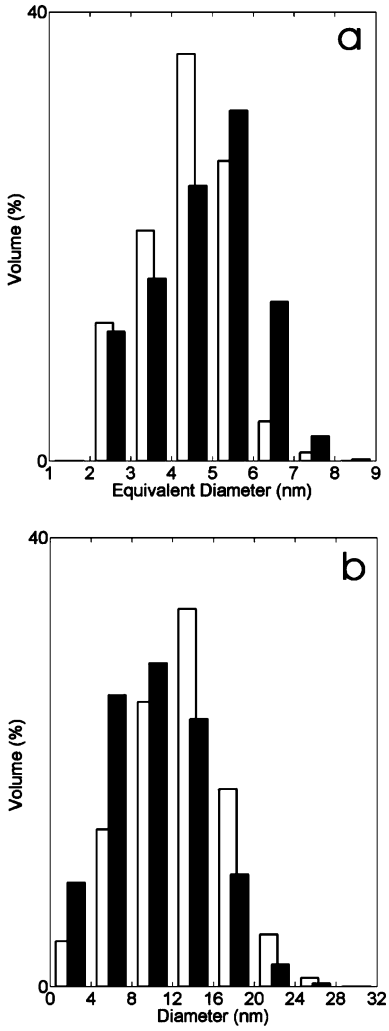

Figure 8. Statistical size distributions of the palladium particles (a) and the silica skeleton (b). The white bars are for Pd1.1, and the black bars are for Pd3.1.

Table 2. Characteristics of Samples Pd1.1 and Pd3.1 Estimated from Image Analysis

sample	Pd1.1	Pd3.1
diameter of Pd particles (nm)	4.4 ± 1.1	4.8 ± 1.3
diameter of Silica skeleton (nm)	12.5 ± 4.8	10.3 ± 4.8
distance from Pd particle to pore surface (nm)	7.9 ± 2.3	6.5 ± 2.0
fraction of free surface of the Voronoi cells	0.39 ± 0.19	0.41 ± 0.22
mean distance to neighboring Voronoi cells (nm)	12.8 ± 5.6	14.6 ± 7.0
number of neighboring Voronoi cells	5.8 ± 2.6	6.4 ± 2.9

3.2. Size Distributions. The size of each palladium nanoparticle can be estimated by its equivalent diameter, i.e., the diameter of the sphere having the same volume. Figure 8a compares the size distribution of the palladium particles of both Pd1.1 and Pd3.1. The particles appear to have very similar sizes in both samples, but slightly larger sizes in Pd3.1 than in Pd1.1, as is reported in Table 2 and which was already found previously using other experimental techniques.[22]

Such a standard granulometry cannot be used to characterize the silica skeleton, because it is made of a

(22) Lambert, S.; C. Alié, Pirard, J.-P.; Heinrichs, B. *J. Non-Cryst. Solids* **2004**, *342*, 70.

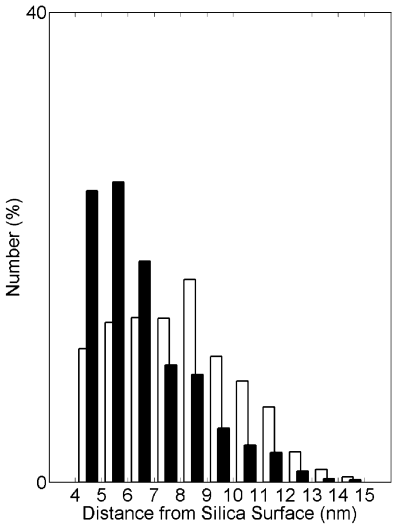

Figure 9. Statistical distributions of the distance between the palladium particles and the surface of the nearest pore. The white bars are for Pd1.1, and the black bars are for Pd3.1.

single object, whose size would be representative of only the crushing of the sample prior to the microscopic observation. A so-called opening size granulometry was therefore performed.[21,23] From this technique, any given pixel of the silica skeleton is said to belong to a structure whose size is the diameter of the largest sphere containing that pixel and being entirely included within the silica. Figure 8b compares the opening size granulometry of samples Pd1.1 and Pd3.1. The most frequent size is slightly smaller for Pd3.1, and the width of the size distribution is almost the same for both samples (Table 2).

3.3. Spatial Distribution of the Pd Nanoparticles. An important aspect of metal dispersion that is difficult to address using physicochemical macroscopic methods is the analysis of the spatial distribution of the metallic particles on or within the support. The qualitative observation of the micrographs suggests that the metallic particles are located inside the silica skeleton (insets of Figure 1). A quantitative characterization is obtained by considering the statistical distribution of the distance between the center of gravity of each Pd nanoparticle and the surface of the nearest pore. These distributions are plotted in Figure 9. In the case of Pd1.1, the distribution has a maximum at a finite distance from the surface, while for Pd3.1, the maximum is nearer to the silica surface. The cutoff in the distributions at ca. 4 nm results from the fact that all particles touching the silica surface have been eliminated during the segmentation (see section 2.3 and parts h and i of Figure 3). The loss of the particles closest to the silica surface is unavoidable with low-resolution tomograms because shadow-like artifacts near the silica surface could not be discriminated from actual particles. The mean value and standard deviation of the distance between Pd and pore space are reported in Table 2.

It is also of interest to assess whether the Pd particles are clustered or uniformly distributed inside the silica. This issue can be addressed by using the concept of influence zones of the particles,[21] also called generalized Voronoi cells.[23] This approach enables determining which particles are neighbors of one another. The analysis is as follows. Around each Pd particle, an influence zone (or a Voronoi cell) is defined as the locus of all points of the silica that are closer to that particle than to any other. In this way, the entire silica skeleton is split into as many zones as there are Pd particles. In the present case, the influence zones were defined through the use of the geodesic distance,[21] corresponding to the length of the shortest path *inside the silica skeleton* between that point and the particle. The resulting tessellation of the silica skeleton is illustrated in Figure 10, in which each color corresponds to the zone of influence of a given Pd particle. The main interest of Voronoi tessellation is that it enables the notion of neighborhood to be defined. Two Pd particles are called neighbors if their Voronoi cells share a common boundary. It was noticed that each particle generally has two types of neighbors. Indeed, the total surface of a mean Voronoi cell accounts for approximately 1000 voxels, and there are a few main neighbors with each of which the surface of contact is several hundreds voxels and secondary neighbors with which the surface of contact is only a few tens of voxels. These latter neighbors are generally also more distant than the former. For the following analysis, the Voronoi cells that share less than 50 voxels are considered as not being neighbors.

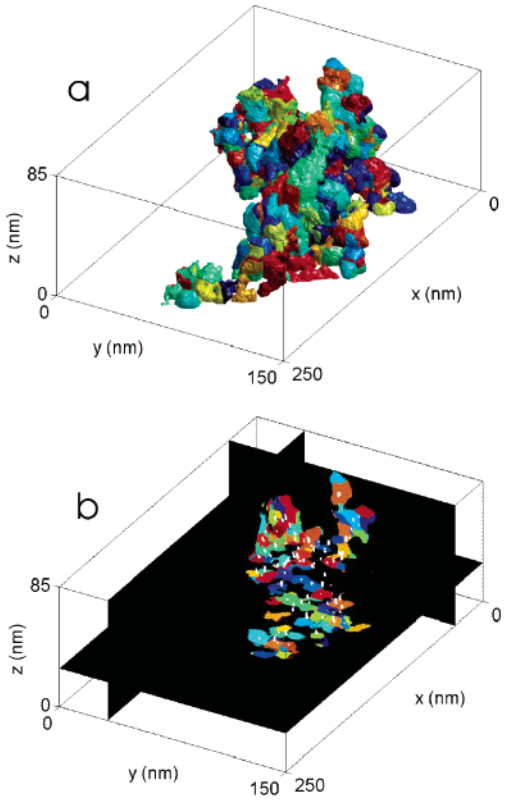

Figure 10. Example of Voronoi tessellation of the silica skeleton of a fragment of Pd1.1 catalyst; each color corresponds to a zone of influence of a specific Pd nanoparticle. (a) Outer surface of the Voronoi cells, and (b) three orthogonal cuts inside the same fragment, with the palladium particles in white.

Figure 11 gathers some statistical distributions derived from the Voronoi tessellation of samples Pd1.1 and Pd3.1. A first quantity of interest is the fraction of the surface of each cell that touches the pore space, with the rest of the surface being in contact with neighboring cells. Figure 11a shows that for most of the cells, approximately 40% of the surface is in contact with pore space (see also Table 2). This means that the structure is quite open and that there are very few Pd particles totally buried under other particles.

The distribution of the mean distance between a particle and all of its neighbors is a parameter that is relevant to the particles dispersion. For instance, in the case of the

(23) Ohser, J.; Mücklich, F. *Statistical Analysis of Microstructures in Materials Science*; Wiley: Chichester, U.K., 2000.

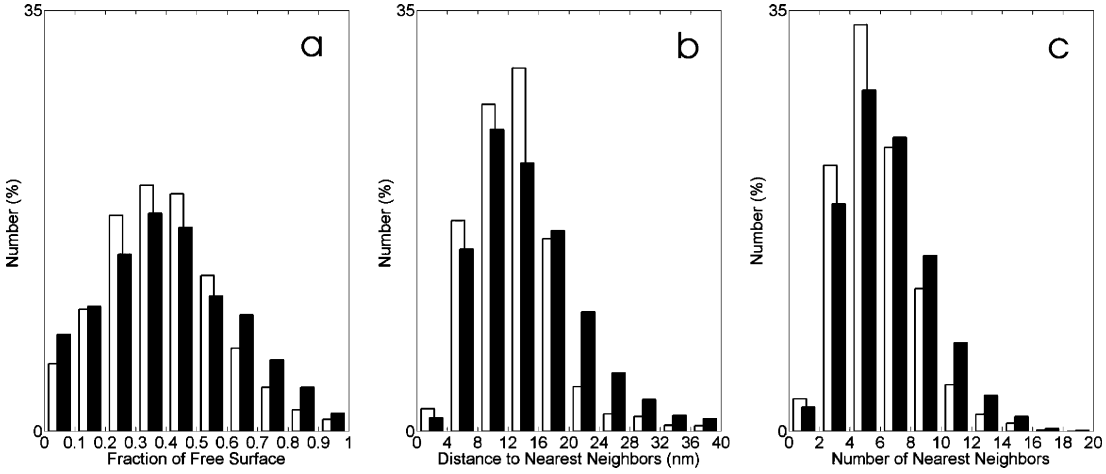

Figure 11. Characteristics of the Voronoi cells: (a) fraction of their surface that is exposed to the pore space, (b) mean distance between neighboring cells, and (c) the number of nearest neighbors. The white bars are for Pd1.1, and the black bars are for Pd3.1.

clustering of the Pd particles, the distribution would be broad because inter- and intracluster distances are expected to be very different. One sees from Figure 11b and Table 2 that the statistical distributions of the mean distance between neighbors are quite narrow, with a standard deviation much smaller than the mean, which means that the particles are well-dispersed in both samples. An interesting observation from Table 2 is that the mean value of the distance between neighboring particles (12.8 and 14.6 nm for Pd1.1 and Pd3.1, respectively) compares reasonably with the size of the silica skeleton estimated by opening granulometry (12.5 and 10.3 nm for Pd1.1 and Pd3.1, respectively).

The number of neighbors of each cell is also interesting to know because it conveys some information on the way in which the particles are spread over the silica (Figure 11c). One, for instance, expects that a large number of neighbors is associated with a large heterogeneity of the spatial distribution. As reported in Table 2, the mean number of neighbors passes from 5.8 to 6.4 from Pd1.1 to Pd3.1.

4. Discussion

The main purpose of this study is the determination of the localization of the palladium particles with respect to the silica skeleton, in heterogeneous catalysts synthesized by the cogelation method. On the basis of mainly 2D TEM observations, it has been sensed for a long time that the smallest metallic particles in these catalysts are located in the middle of the silica skeleton,[1,2,7−11,22] but this conclusion was still questionable because 2D TEM only gives access to projections of the objects. The present use of electron tomography allows a cogent demonstration to be given that indeed the smallest metallic particles are inside the silica skeleton. The present analysis also confirms that the very large particles that appear for high metal loadings are mainly located at the surface of the silica skeleton. It is important to stress that the small Pd particles are fully accessible, despite their being inside the silica skeleton. Nitrogen adsorption measurements performed on these catalysts[22] reveal a significant amount of very small pores, whose size is comparable to that of the nitrogen molecule. Obviously, these pores went undetected on the used low-resolution tomograms, and the segmented silica phase is actually microporous.

The use of low-resolution tomograms enables a statistically representative amount of metallic particles (about 3000 per sample) to be handled. The resolution of the tomograms can be roughly estimated as the ratio of the thickness of the sample to the number of projections used for the reconstruction.[17] Considering that the samples are about 100 nm thick and that 140 projections are used (section 2.2), the resolution is expected to be of the same order of magnitude as the size of the Pd particles. The difference between the actual size of the particles, as assessed by chemisorption, and the size estimated by image analysis is also of the same order of magnitude, about 2 nm. Even if the size of the particles is close to the resolution, their contrast with the silica is sufficient for their unambiguous localization (e.g., see Figure 1 or Figure 2a). Furthermore, once the particles are localized, the low resolution is not expected to bias the estimation of the distances between themselves or to the surface of the silica skeleton.

For sample Pd1.1, the metal loading estimated from image analysis (about 3 wt %) slightly overestimates the macroscopic metal loading (1.1 wt %), but it is however of the same order of magnitude. This suggests that most of the palladium in that specific sample is under the form of nanoparticles located inside the silica. The overestimation results from an artificial elongation of the metallic particles because of the limited angular range in single axis tomography. This overestimation of the size of the Pd nanoparticles is also visible when their size estimated by image analysis, 4.4 nm (Table 2), is compared with the size estimated from CO chemisorption, 2.7 nm, according to ref 7. The same artifact is also present in the tomograms of sample Pd3.1. This is the reason why, despite the presence of very large metallic particles not taken into account in the statistics, the metal loading of that sample is not severely underestimated by image analysis. For that sample, chemisorption predicts a size of 4.6 nm,[7] but this value is an average of the size of the small particles inside the silica and the very large particles on its surface.

The present analysis and notably the use of Voronoi tessellation enables clear conclusions to be drawn on the statistical localization of the particles. First, it is particularly interesting to note that the diameter of the silica skeleton and the distance between neighboring palladium particles are almost identical for Pd1.1 (Table 2). Second, the distance between the palladium particles and the silica surface is approximately half of the aforementioned distance. These two observations show that the palladium particles in Pd1.1 are almost regularly distributed in the middle of the struts of the silica skeleton. In that respect, the results of the present image analysis are in agreement

with an early simplified geometrical model of the catalysts with low metal loading, according to which the palladium particles would be in the center of silica particles.[1]

The spatial distribution of the small Pd particles also evolves when the metal loading is increased. As already known from other studies,[7,22] the size of the silica skeleton decreases when more metal (and consequently EDAS) is used, which is also observed when EDAS is used alone, without any metallic salt.[24] Because the distance between the particles and the surface of the silica follows the same trend (Table 2), it seems that the palladium particles could still be in the middle of the silica skeleton for Pd3.1. It is interesting to note that the detected particles in Pd3.1 are on average more distant from one another than those in Pd1.1, notwithstanding the smaller dimension of the silica skeleton. Also, the mean number of neighbors, as well as the width of the distribution of distance between neighbors, is larger in Pd3.1 than in Pd1.1 (Table 2), which suggests that the dispersion of palladium in Pd3.1 is less homogeneous.

The mechanisms by which the unique structure of Pd1.1 forms, with the palladium nanoparticles optimally dispersed inside the silica skeleton, are unclear yet. It was initially surmised that EDAS polymerized before TEOS, because of the presence of methoxy groups that are more reactive toward hydrolysis than the ethoxy groups of TEOS, leading thereby to the creation of organometallic nuclei around which TEOS could polymerize.[1] This mechanism would however not explain why an increasing amount of metal would be located outside of the silica when the loading is increased, as, e.g., in Pd3.1. Furthermore, it was shown using time-resolved small-angle X-ray scattering that the structure of materials synthesized from TEOS and EDAS without any metal forms via a phase separation process that is likely to be driven by physical forces.[25] A further textural analysis of these metal-free samples suggested that the amount of EDAS on the surface of the silica increases with the total amount of EDAS, which might be related to the fact that this molecule can also act as a surfactant in the phase separation process.[26] The main two characteristics of samples Pd1.1 and Pd3.1 might therefore be related to the dual role of EDAS. The good dispersion of palladium within the silica is understandable from the larger reactivity of the methoxy groups of the Pd−EDAS complex compared to the ethoxy groups of TEOS. The increasing amount of palladium outside of the silica in Pd3.1 could result from the role that EDAS plays in the phase separation process.

5. Conclusions

It has been shown in this study that catalysts synthesized by the cogelation of tetraethoxysilane and of a 3-(2-aminoethylamino)propyltrimethoxysilane−palladium complex are characterized by nanometric metallic particles located deep inside the silica skeleton. The use of digital image analysis enables quantitative conclusions to be drawn from the electron tomograms. For the catalyst with the lowest metal loading, the palladium particles are optimally dispersed in the middle of the struts of the silica support, with distances between them comparable to the width of the struts. For the sample with a larger metal loading, the same conclusion holds qualitatively for those particles inside of the silica, but a significant fraction of the metal seems to be located outside of the silica.

Acknowledgment. C. J. G. is grateful to the FNRS (National Funds for Scientific Research, Belgium) for a Ph.D. research fellow position. The authors thank Dr. Benoît Heinrichs and Dr. Stéphanie Lambert of the University of Liège for fruitful discussions. This work was supported by the Fonds de Bay, the Fonds de la Recherche Fondamentale et Collective, the Ministère de la Communauté Française de Belgique (ARC 00/05-265), and the Ministère de la Région Wallonne. The authors also acknowledge the involvement of their laboratory in the network of excellence FAME of the European Union 6th framework program.

LA051682C

(24) Alié, C.; Pirard, R.; Lecloux, A. J.; Pirard, J.-P. *J. Non-Cryst. Solids* **1999**, *246*, 216.

(25) Gommes, C. J.; Blacher, S.; Goderis, B.; Pirard, R.; Heinrichs, B.; Alié, C.; Pirard, J.-P. *J. Phys. Chem B* **2004**, *108*, 8983.

(26) Gommes, C. J.; Blacher, S.; Basiura, M.; Goderis, B.; Pirard, J.-P. *J. Phys. Chem. B*, manuscript submitted for publication.